ACS NANO

www.acsnano.org

ARTICLE

Overcoming High-Quality Limitations in Plasmonic Metasurfaces for Ultrasensitive Terahertz Applications

Ziheng Ren, Yuze Hu,* Weibao He, Shun Wan, Siyang Hu, Zhongyi Yu, Xiang'ai Cheng, Zhongjie Xu,* and Tian Jiang*

Cite This: *ACS Nano* 2024, 18, 21211−21220

Read Online

ACCESS | Metrics & More | Article Recommendations | Supporting Information

ABSTRACT: In photonics, achieving high-quality (Q) resonance is crucial for high-sensitivity devices used in applications, such as switching, sensing, and lasing. However, high-Q resonances are highly susceptible to internal losses of plasmonic devices, impeding their integration into broader systems across terahertz and visible light bands. Here, we overcome this challenge by proposing a low-Q plasmonic metasurface for ultrasensitive terahertz (THz) switching and sensing. Theoretically, we reveal an approach to constructing a low-Q resonator possessing high sensitivity to nonradiative losses. Leveraging this mechanism, we design a highly sensitive plasmonic metasurface induced by strong coupling between a quasi-bound state in the continuum and a dipole mode. By hybridizing with the germanium layer, the metadevice exhibits an ultralow pump threshold of 192 $\mu J/cm^2$ and an ultrafast switching cycle time of 7 ps. Furthermore, it also shows a high sensitivity of 224 GHz/RIU in refractive index sensing. The proposed paradigm of constructing low-Q and high-sensitivity photonic devices can be applied to biosensing, wide-band filters, and sensitive modulators.

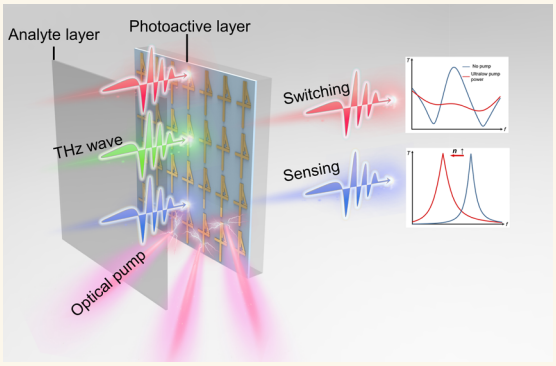

KEYWORDS: *high sensitivity, terahertz, metasurfaces, ultrafast switching, bound states in the continuum, quality factor*

In photonics, high-quality (Q) resonances have garnered significant interest due to their pivotal role in sensitive devices. The features, such as narrow linewidth, long photon lifetime, and energy storage capability, make high-Q resonators highly desirable for diverse applications, including sensing,[1] lasing,[2] and nonlinear optics.[3] In subwavelength micro/nanostructures, the significance of high-Q resonances arises from the ability to confine light in extremely small volumes, thereby fostering intensified light−matter interactions.[4,5] Despite numerous advantages, high-Q resonances also present specific challenges that require careful consideration. The realization of high-Q resonances often necessitates ultralow material losses, such as dielectric platforms.[6−10] However, this limitation hinders the development of high-Q resonances to broader systems such as plasmonic platforms suffering from inherent Ohmic losses. Simultaneously, low-Q factors resulting from Ohmic losses make plasmonic devices insensitive and unsuitable for practical applications. Although existing efforts explore ways to achieve high-Q resonances in plasmonic structures as a means to tackle this challenge,[11−14] engineering a high-sensitive device within the realm of low-Q resonances remains unexplored, requiring intensive attention.

Within the broader context of photonics, the terahertz (THz) frequency,[15] ranging from 0.1 to 10 THz, has recently attracted considerable interest due to its unique properties. This spectrum holds great promise for applications in various fields, including communication,[16,17] imaging,[18] spectroscopy,[19] security detection,[20] and sensing.[21−25] Recently, metasurfaces have revolutionized THz photonics by providing efficient control over THz waves.[26] By precisely tailoring the subwavelength-scale meta-atoms within metasurfaces, it is possible to modulate the phase,[27] amplitude,[28] and polarization[29] of THz waves. The fixed structure of the metasurfaces solidifies their functionality, so the quest for dynamic modulation is critical in unlocking further potential within this technology.[30] Dynamically controllable components, such

Received: April 7, 2024
Revised: July 11, 2024
Accepted: July 17, 2024
Published: July 30, 2024

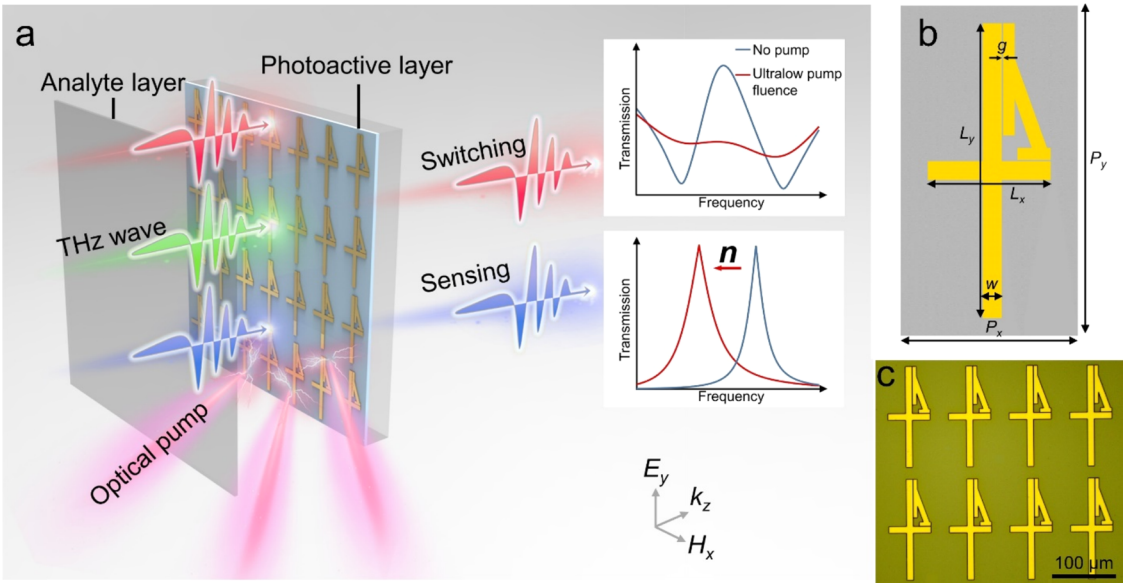

Figure 1. Schematic of the ultrasensitive quasi-BIC metasurface driven by strong mode coupling. (a) Working principle of the metasurface for ultrasensitive switching and sensing. The metasurface is composed of a resonant gold layer and a quartz substrate. To achieve dynamic modulation, the metasurface is hybridized with a photoactive Ge layer, and the photocarrier concentration in Ge is controlled by an optical pump knob. For sensing, the analyte layer is uniformly coated onto the surface of the metasurface. (b) The geometric parameters of the meta-atom: P_x = 75, P_y = 140, L_x = 52, L_y = 125, w = 8, and g = 0.5 μm. (c) Optical microscope image of the fabricated metasurface. Scale bar: 100 μm.

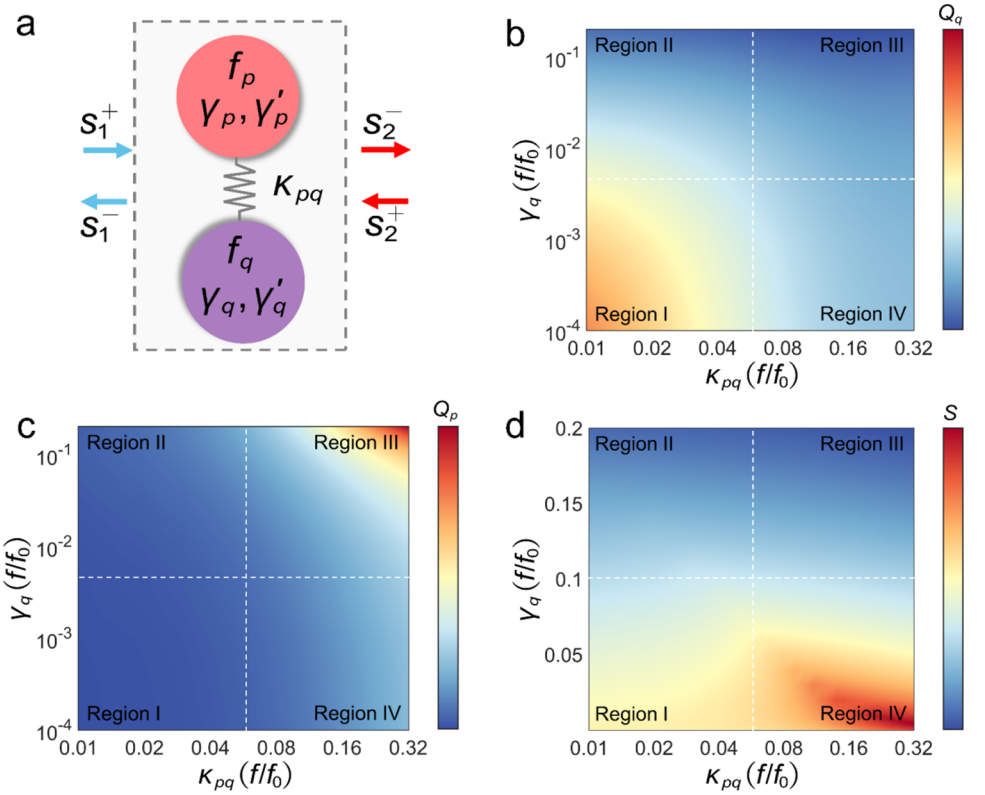

Figure 2. Phase diagrams for the two-port, two-mode coupling system. (a) Schematic of the coupled systems. f_i, γ_i, γ_i', $\kappa_{pq}(i = p,q)$ are the resonant frequency, radiative losses, nonradiative losses, and near-field coupling, respectively. Uncoupled mode "p" is a low-Q mode with high radiative losses of $\gamma_p = 0.2f_0$. Phase diagrams of the Q factor of coupled bonding modes (b) "q" and (c) "p," and (d) the system's sensitivity to nonradiative losses. Each phase diagram can be qualitatively divided into four regions: Region I, low γ_q, weak κ_{pq}; Region II, high γ_q, weak κ_{pq}; Region III, high γ_q, strong κ_{pq}; Region IV, low γ_q, strong κ_{pq}. In Region IV, both coupled modes "p" and "q" exhibit low Q factors, and the resonator exhibits enhanced sensitivity to nonradiative losses.

as two-dimensional semiconductors,[31−33] liquid crystals,[34] phase change materials,[35,36] graphene,[37] and transition metal dichalcogenides,[38] can be modulated by external stimuli such as optical pumping,[39−41] voltage- or current-bias,[36,42,43] and

https://doi.org/10.1021/acsnano.4c04565
ACS Nano 2024, 18, 21211−21220

temperature,[44] thereby offering the potential for reconfigurable THz metadevices. On the other hand, widely used terahertz systems, such as Terahertz time-domain spectroscopy (THz-TDS) systems, are not compatible with high-Q devices due to limited spectral resolution.[45,46] This limitation constrains the practical applications of high-Q resonators and significantly impedes the advancement of terahertz technology. Thus, it is essential to reassess the potentiality of low-Q resonators possessing high compatibility with the THz-TDS system.

Here, we experimentally demonstrate a highly sensitive, low-Q THz reconfigurable plasmonic THz metasurface based on our proposed theoretical framework. Theoretically, it is found that a low-Q resonator with high sensitivity to nonradiative losses can be achieved by facilitating the coupling between two specific modes. Utilizing this concept, a quasi-bound state in the continuum (quasi-BIC) metasurface is constructed, wherein a nanogap facilitates the mode coupling. This strategy serves to significantly reduce the Q factor of the quasi-BIC, simultaneously enhancing both the sensitivity and near-field strength within the metasurface. Subsequently, we achieve dynamically controllable functionality by hybridizing the metasurface with a germanium (Ge) layer. Notably, in the ultrafast THz switching with a time scale of several picoseconds, the pump threshold is as low as 192 $\mu J/cm^2$, an order of magnitude lower than analogous works (>1100 $\mu J/cm^2$).[33,47−52] Furthermore, benefiting from large near-field enhancement, the metasurface demonstrates a high sensitivity of 224 GHz/RIU in refractive index sensing. This work presents an approach to overcoming high-Q limitations in plasmonic metasurface for ultrasensitive THz switching and sensing, offering a pathway toward developing highly sensitive, tunable THz metadevices compatible with existing photoelectronic devices (Figure 1)

RESULTS AND DISCUSSION

Theoretical Model. In the realm of photonics, researchers are relentlessly pursuing advancements in the Q factor of resonators, which is a pivotal element for enhancing the light−matter interactions in photonic devices. Nonetheless, when delving into the realm of plasmonic nanostructures, there exists a formidable obstacle. The resistive loss inherent to plasmonic structures serves as a bottleneck, impeding progress in elevating the Q factor to the desired levels. Here, we aspire to reveal a paradigm for enhanced light−matter interaction, transcending the traditional reliance on high Q factors alone. Following this, we establish a two-mode, two-port coupling resonant system, as illustrated in Figure 2a, grounded in temporal coupled-mode theory (CMT), to facilitate deeper exploration. Based on the Hamiltonian formalism,[53,54] the coupled system is described in terms of two eigenmodes: "p" and "q." The Hamiltonian is provided by $\mathbf{H}|\Psi_i\rangle = 2\pi f_i |\Psi_i\rangle$ $(i = p,q)$. The total wave function of the system is regarded as the linear combination of the wave function of each mode: $|\Psi\rangle = a_p|\Psi_p\rangle + a_q |\Psi_q\rangle$, where a_p and a_q are the amplitudes of two resonance modes, respectively. Then, the amplitudes of two resonant modes in the open system can be described as

$$\frac{1}{2\pi}\frac{\partial}{\partial t}\begin{pmatrix} a_p \\ a_q \end{pmatrix} = -i\left[\begin{pmatrix} f_p & \kappa_{pq} \\ \kappa_{qp} & f_q \end{pmatrix} - i\begin{pmatrix} \gamma_p' & 0 \\ 0 & \gamma_q' \end{pmatrix}\right]\begin{pmatrix} a_p \\ a_q \end{pmatrix} - \begin{pmatrix} \gamma_p & X \\ X & \gamma_q \end{pmatrix}\begin{pmatrix} a_p \\ a_q \end{pmatrix} + \begin{pmatrix} d_{1p} & d_{2p} \\ d_{1q} & d_{2q} \end{pmatrix} S^+ \tag{1}$$

$$S^- = \begin{pmatrix} r_{sub} & t_{sub} \\ t_{sub} & r_{sub} \end{pmatrix} S^+ + \begin{pmatrix} d_{1p} & d_{1q} \\ d_{2q} & d_{2p} \end{pmatrix}\begin{pmatrix} a_p \\ a_q \end{pmatrix} \tag{2}$$

where f_i, $\gamma_i (i = p,q)$ are the resonant frequencies and radiation losses, which have been seen as the intrinsic parameters of modes. γ_i' $(i = p,q)$ presents the nonradiation losses, mimicking the loss-induced active modulation. κ_{pq} and κ_{qp} present the near-field coupling coefficients of two eigenmodes, and they are conjugate to each other. $S^i = [S_1^i, S_2^i]^T (i = +, -)$ denotes the strength of incoming (+) and outgoing (−) waves of port 1 and port 2, and d_{ij} $(i = 1, 2; j = p,q)$ represents the couplings between the excitation of the external port (1 or 2) and radiative mode ("p" or "q"). r_{sub} and t_{sub} are the reflection and transmission amplitudes of the substrate, constituting the background scattering matrix between two ports without resonant modes. Based on energy conservation and time-reversal symmetry, we get

$$\begin{pmatrix} r_{sub} & t_{sub} \\ t_{sub} & r_{sub} \end{pmatrix}\begin{pmatrix} d_{1p} & d_{1q} \\ d_{2p} & d_{2q} \end{pmatrix}^* = -\begin{pmatrix} d_{1p} & d_{1q} \\ d_{2q} & d_{2q} \end{pmatrix} \tag{3}$$

$$-\frac{1}{2}\begin{pmatrix} d_{1p} & d_{1q} \\ d_{2q} & d_{2q} \end{pmatrix}^\dagger\begin{pmatrix} d_{1p} & d_{1q} \\ d_{2p} & d_{2q} \end{pmatrix} = \begin{pmatrix} -\gamma_p & X \\ X & -\gamma_q \end{pmatrix} \tag{4}$$

For further analysis and solution through standard CMT, the transmission coefficients from port 1 to port 2 are given by solving eqs 1−4

$$t = \frac{S_2^-}{S_1^+} = F(f_i, \gamma_i, -\gamma_i', \kappa_{pq})(i = p, q) \tag{5}$$

where the detailed expression of eq 5 is shown in Supporting Information Note 1. The multiple physical parameters in this equation enable us to delve into and uncover fascinating phenomena in the coupled system. It is necessary to discuss how these parameters impact the Q factors of coupled bonding modes and the system's sensitivity to nonradiative loss perturbations. The Q factor of resonance is defined as

$$Q = \frac{f}{\Delta f} \tag{6}$$

where f is the resonant frequency and Δf is the full width at half maximum of the resonance. The theoretical sensitivity of the resonator to nonradiative losses is defined as

$$S = \frac{1}{\gamma'_{T_{dip}=0.5}} \tag{7}$$

where $\gamma'_{T_{dip}} = 0.5$ represents the value of the nonradiative losses when both transmission coefficients of resonance dips achieve 0.5. A large S signifies that weak nonradiative loss injection can induce a great modulation depth, beneficial to the design of optical THz switches with low thresholds.

https://doi.org/10.1021/acsnano.4c04565
ACS Nano 2024, 18, 21211−21220

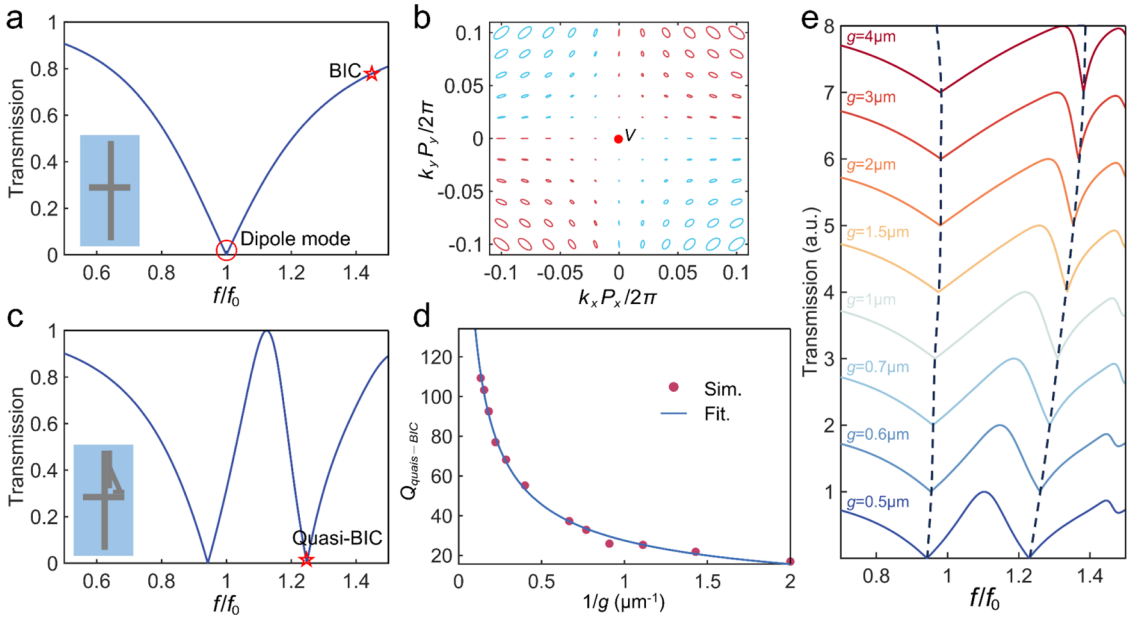

Figure 3. Implement of the low-Q metasurface. (a) Transmission spectrum of the cruciform meta-atom (inset), which supports a dipole mode (red circle) and a symmetry-protected BIC (red star). (b) Far-field polarization states near the BIC (*V* point) in momentum space. (c) Transmission spectrum of the meta-atom in which the asymmetric perturbation is introduced to break the in-plane C_2 symmetry, BIC transitions into quasi-BIC, nanogap width $g = 0.5\ \mu m$. (d) Q factor of quasi-BIC diverges as a function of nanogap widths *g*. (e) Transmission spectra for different nanogap widths. A smaller gap width *g* means stronger coupling, resulting in a wider line width of quasi-BIC.

By tuning the radiation losses γ_q of mode "q" and near-field coupling κ_{pq}, we get the phase diagrams of the coupled bonding modes' Q factors, Q_p, Q_q, and the sensitivity *S*, respectively, as shown in Figure 2b–d. Here, uncoupled mode "p" is set as a low-Q mode with a high radiation loss of $\gamma_p = 0.2f_0$ and a resonant frequency of $f_p = 0.9f_0$. Mode "q" with a resonance frequency $f_q = 1.1f_0$ has varying radiation rates.

We qualitatively divide each phase diagram into four regions to discuss, which correspond to four conditions of the resonant system. In Region I, mode "q" holds tiny radiation losses and weak coupling with the low-Q mode "p," exhibiting a high Q factor, as shown in Figure 2b. Maintaining constant coupling and increasing the radiation losses of mode "q," the system transitions into Region II. In this regime, both the Q_q and *S* exhibit a decline relative to those observed in Region I. This trivial region corresponds to the case when two low-Q modes are weakly coupled in a resonant system. In Region III, both γ_q and κ_{pq} are high, indicating that two modes with high radiation losses are strongly coupled. However, this case does not necessarily enhance the resonator's sensitivity significantly, instead, resulting in a high Q_q. This regime is undesirable and should be avoided in the design of low-Q resonators. It is worth noticing Region IV, which indicates that a low-radiation rate mode "q" and a high-radiation rate mode "p" are strongly coupled. This strong coupling effect not only converts mode "q" into the low-Q mode but also improves the *S*. This intriguing phenomenon provides a fascinating possibility of realizing highly sensitive active modulators with low Q factors, consistent with our aspirations.

Implement of Low-Q Quasi-BIC Metasurface. In the following, based on the theoretical framework, we design a low-Q metasurface working in Region IV of Figure 2b–d. Considering the prerequisites to construct the desired resonator, a high-radiation rate mode and a low-radiation rate mode must be supported by the metasurface. The building block of the metasurface is configured with a cruciform geometry (inset in Figure 3a). This structure with in-plane C_2 symmetry can host a low-Q dipole mode (red circle) and a symmetry-protected BIC without radiation losses (red star), as shown in Figure 3a. The far-field polarization states near the BIC within the momentum space are shown in Figure 3b. The red and blue ellipses represent the eigen right-handed and left-handed far-field polarization states, respectively. As a vortex-like singularity (*V* point) with an undefined polarization state, the BIC cannot radiate outward to the far-field.[55,56] Nevertheless, the BIC can transition into high-Q quasi-BIC with low radiative losses by breaking structural symmetry or mismatching the mode coupling condition.[57,58]

Subsequently, we disrupt the in-plane C_2 symmetry by introducing asymmetric perturbation (inset in Figure 3c), and the spatially symmetric field distribution of the BIC is consequently broken. This leads to the BIC leaks to quasi-BIC, as shown in Figure 3c. The nanogap between the cruciform structure and asymmetric perturbation, with a width denoted as *g*, as shown in Figure 1b, plays a key role in controlling the coupling of the dipole mode and quasi-BIC. The narrower the gap width, the stronger the coupling. As shown in Figure 3d,e, during the reduction of *g*, the *Q*-factor of quasi-BIC experiences a gradual decrease, accompanied by a broadening of its spectral line width.

Metasurface Fabrication and Ultrasensitive Photon-induced Modulation. The above-mentioned have successfully demonstrated the achievement of low-Q metasurface through strong coupling of quasi-BIC and dipole mode. Next, we incorporate a photoactive Ge layer into the metasurface to endow it with dynamic reconfigurability. This material is selected due to its favorable bandgap (0.66 eV) and carrier mobility properties. The hybrid metasurface consists of a 200 nm-thick layer of lossy gold and a 300 nm-thick layer of amorphous Ge. The schematic of the meta-atom is shown in Figure 1b, with well-optimized dimensions: $P_x = 75$, $P_y = 140$, $L_x = 52$, $L_y = 125$, $w = 8$, and $g = 0.5\ \mu m$. An optical

https://doi.org/10.1021/acsnano.4c04565
ACS Nano 2024, 18, 21211–21220

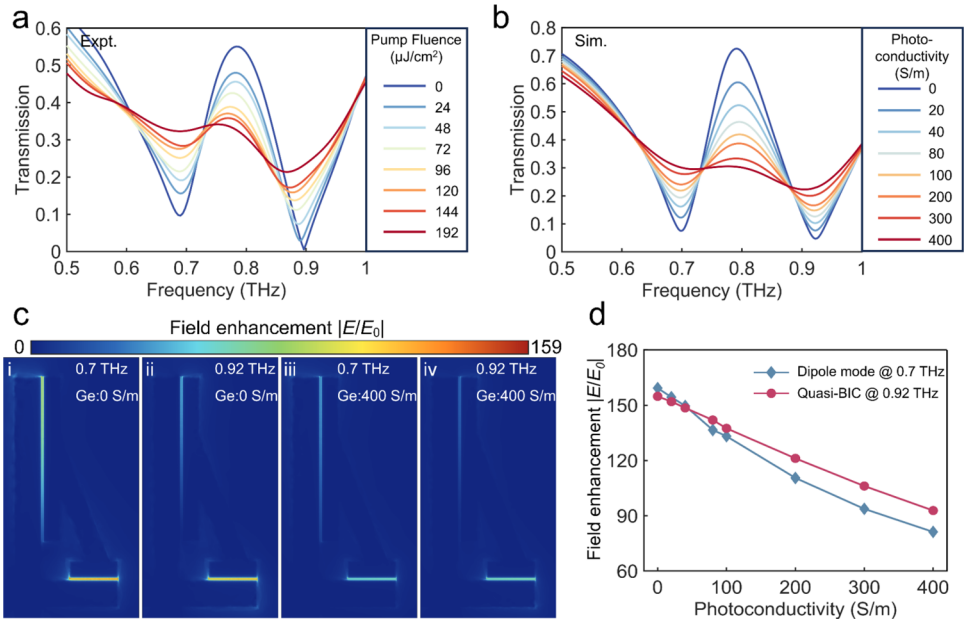

Figure 4. Ultrasensitive photoinduced modulation and near-field enhancement of the metasurface. (a) Measured transmission spectrum with different pump fluence. The pump threshold to switch the metasurface is as low as 192 μJ/cm^2, an order of magnitude reduction compared to previous similar works (≥1100 μJ/cm^2). (b) Numerical simulated transmission spectrum responses as a function of the photoconductivity of Ge. (c) Distribution maps of the near-field enhancement ratios for the upper right section of the metasurface, at the frequencies of dipole mode (0.7 THz) and quasi-BIC (0.92 THz) with the photoconductivity of Ge of (i–ii) 0 and (iii, iv) 400 S/m. (d) The maximum near-field enhancement ratios at 0.7 and 0.92 THz as a function of the photoconductivity of Ge.

microscope image of the fabricated metasurface is shown in Figure 1c. The Ge layer and gold layer are deposited on the quartz substrate uniformly, and then, gold structures are etched using ion beam etching (IBE) technology (the detailed process is shown in the Methods Section).

To validate the photon-induced modulation properties of the Ge-hybrid metasurface, we initiated the characterization process using the THz-TDS systems. The THz pulse is incident on the sample in a normal direction (k_z), with its polarization along the long side of the cruciform structure (E_y). Femtosecond optical pulses with durations of 100 fs and a wavelength of 800 nm possess photon energies exceeding the bandgap of amorphous Ge, thereby enabling the efficient pump of carriers from the valence band to the conduction band and consequently inducing dynamic photoconductivity. These photoexcited carriers induce absorption losses within the resonant cavity, concurrently suppressing both the quasi-BIC and dipole resonances, resulting in the effective modulation of transmission amplitude.

The experimental result of the photon-induced modulation effect on the transmission spectrum of the metasurface is presented in Figure 4a. The transmission spectrum manifests a Fano resonance featuring two dips positioned at frequencies of 0.69 and 0.9 THz, corresponding to the dipole and the quasi-BIC resonances, respectively. Significantly, the transmission amplitudes exhibit high variability with a slight increase in pump fluence, underscoring the ultrasensitive susceptibility to photocarrier injection. As the pump fluence incrementally rises, the transmission amplitudes at the dipole and quasi-BIC resonances gradually ascend, while the Fano peak descends. At 192 μJ/cm^2, the resonance of the dipole mode is annihilated, and the transmission difference between the dipole resonance and Fano peak approaches zero, presenting the annihilation of Fano resonance. The pump threshold to switch this metasurface represents an order of magnitude reduction compared to other optical-controlled Ge metasurfaces (>1100 μJ/cm^2), as shown in Figure 6f. This metasurface exhibits a higher sensitivity to photoconductivity perturbation than other studies, highlighting its superior performance and potential for sensitive photonic applications.

As depicted in Figure 4b, the simulated results match well with the measured results, and the Fano resonance undergoes complete deactivation when the photoconductivity is raised to a mere 400 S/m. In numerical simulations, the photoconductivity is modeled as an adjustable parameter that reflects the concentration of photocarriers in Ge, allowing us to mimic the effects of optical pumping. Notably, the experimental transmission amplitudes exhibit a decrease compared to the simulated results, potentially attributed to the lower experimental conductivity of gold in contrast to the simulation settings (4.52×10^7 S/m).

The nanogap within the metasurface generates significant field enhancement and light confinement. This phenomenon dramatically facilitates the interaction between light and matter and the sensitivity of the metasurface. In Figure 4c(i), at 0.7 THz, the metasurface achieves a 159-fold maximum field enhancement. Furthermore, the localized field is highly susceptible to nonradiative losses, which can reduce the confinement efficiency of light. As depicted in Figure 4c, near-field enhancement $|E/E_0|$ is predominantly localized within the nanogap. The introduction of 400 S/m photoconductivity notably attenuates the near-field enhancement ratio, leading to the annihilation of the resonance. Moreover, the maximum near-field enhancement ratios of the two resonances at 0.7 and 0.92 THz decrease linearly with the increase of the photoconductivity of Ge, as shown in Figure 4d. The intensified local fields can significantly boost light–matter

https://doi.org/10.1021/acsnano.4c04565
ACS Nano 2024, 18, 21211–21220

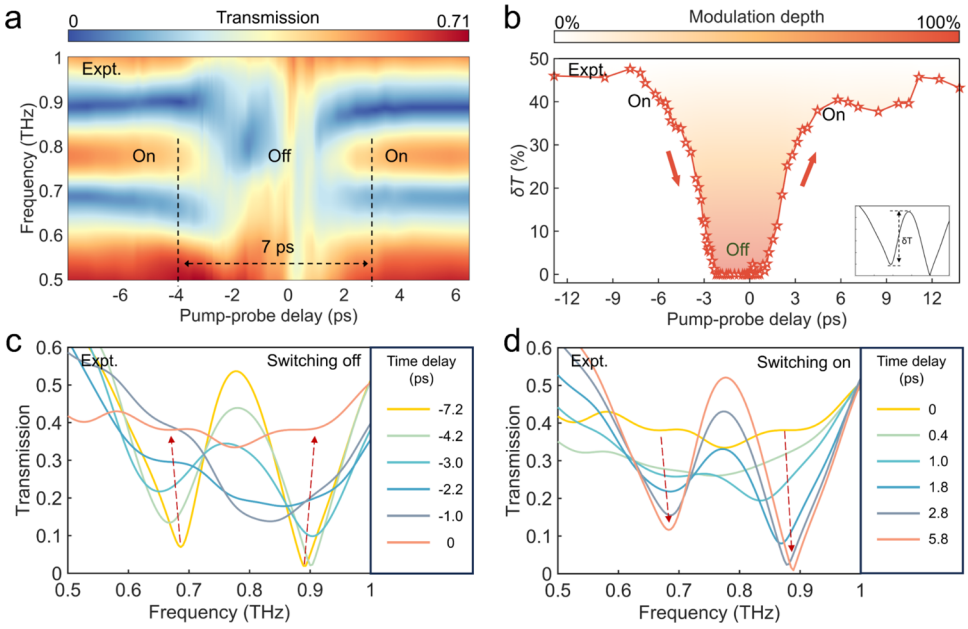

Figure 5. Measured transient dynamics of ultrafast metasurface switching. (a) Color-coded map of the variation in THz transmission amplitude across different frequencies and pump−probe time delays throughout the ultrafast On−Off−On photoswitching cycle within a time scale of picoseconds. (b) Transient peak-to-dip amplitudes δT of the Fano resonance and normalized modulation depth map as a function of pump−probe time delay. Detailed evolution of transmission spectra during metasurface (c) switching off and (d) switching on at several pump−probe time delays.

interactions, making it possible to design compact devices for frequency mixing, harmonic generation, and sensing.

Ultrafast THz Switching. By harnessing the transient photocarrier excitation and relaxation of two-dimensional semiconductor materials, achieving ultrafast tunability and switching in the temporal domain in THz metadevices becomes feasible. This technology gives possibilities for utilization in THz communication and ultrafast photonics research. The following will showcase the ultrafast switching function of the Ge-hybrid metasurface by varying the pump−probe time delay of the optical pump and THz probe (OPTP) systems (for a detailed measurement, see Methods Section).

We first measure the ultrafast photocarrier excitation and relaxation dynamics of the 300 nm-thick amorphous Ge film using the OPTP systems at selected pump fluences,[59] as shown in Figure S1 (Supporting Information Note 2). The measured transient differential transmission ($-\Delta E/E_0$) of THz pulse passing through the Ge film versus pump−probe time delays reflects the ultrafast carriers' excitation and relaxation process. This whole process is about 3 ps, with the photocarrier lifetime of $\tau < 0.7$ ps, where E_0 is the maximum peak amplitude of the THz electric field and ΔE is the attenuation value of E_0. Generally, such an ultrafast photocarrier relaxation is treated as a transient perturbation of the metasurface resonant cavity.

Figure 5a presents the measured transmission spectra map of the metasurface concerning the pump−probe time delays, where the pump fluence is 560 μJ/cm^2. It illustrates how the THz spectrum undergoes a switching process under dynamic modulation of the hybrid metasurface, starting from activation ("On" state) to deactivation ("Off" state) and then back to activation ("On" state) as the time delay changes from −4 to 3 ps. This complete on−off−on switching cycle spans a duration of 7 ps, which is faster than other works, as shown in Figure 5f. To quantify the properties of the ultrafast switching, we define $\delta T = (T_{peak} - T_{dip}) \times 100\%$ and $D = (\delta T_{passive} - \delta T_{pump})/\delta T_{passive} \times 100\%$ as the peak-to-dip amplitudes (inset in Figure 5b) and the normalized modulation depth. When the resonance dip is higher than the peak, the resonance attenuates, and δT equals zero, and D reaches 100%. Figure 5b illustrates the variation of δT in response to the pump−probe time delay. As the time delay transitions from −8 to −2.4 ps, δT rapidly decreases from 48 to 0%. This is succeeded by a phase where the Fano resonance is entirely deactivated within the −2.4 to 1 ps range. Subsequently, as the optical pump is incrementally separated from the THz pulse, the Fano resonance re-emerges, leading to an increase in δT. Furthermore, Figure 5b also quantitatively identifies the modulation depth within the range from 0 to 100%. In this visualization, the shade of the gradient color is indicative of the magnitude of the modulation depth. Figure 5c,d shows the detailed evolution of transmission spectra during the metasurface switching off and switching on at several selected pump−probe time delays. This high-speed, low-energy threshold THz switching is an ideal candidate for efficient THz spatial communication devices.

High-Sensitivity THz Refractive Index Sensor. Resonant electromagnetic excitation gives rise to both temporal and spatial energy confinement within a resonator structure. Temporally, this confinement is manifested through the spectral line width of the resonance, serving as a proxy for the photon lifetime within the cavity and thereby defining the cavity's Q factor. Spatially, the degree of confinement is intrinsically linked to the photon density, which is, in turn, influenced by the intensity of the resonance. Investigations in the meta-sensor domain have predominantly centered on the quest for high-Q resonators to facilitate long-lasting light−matter interaction. However, high-Q devices are impractical in the THz regime. In contrast to approaches of extended temporal confinement, our research employs a nanogap to enhance spatial confinement, effectively boosting the photon

https://doi.org/10.1021/acsnano.4c04565
ACS Nano 2024, 18, 21211−21220

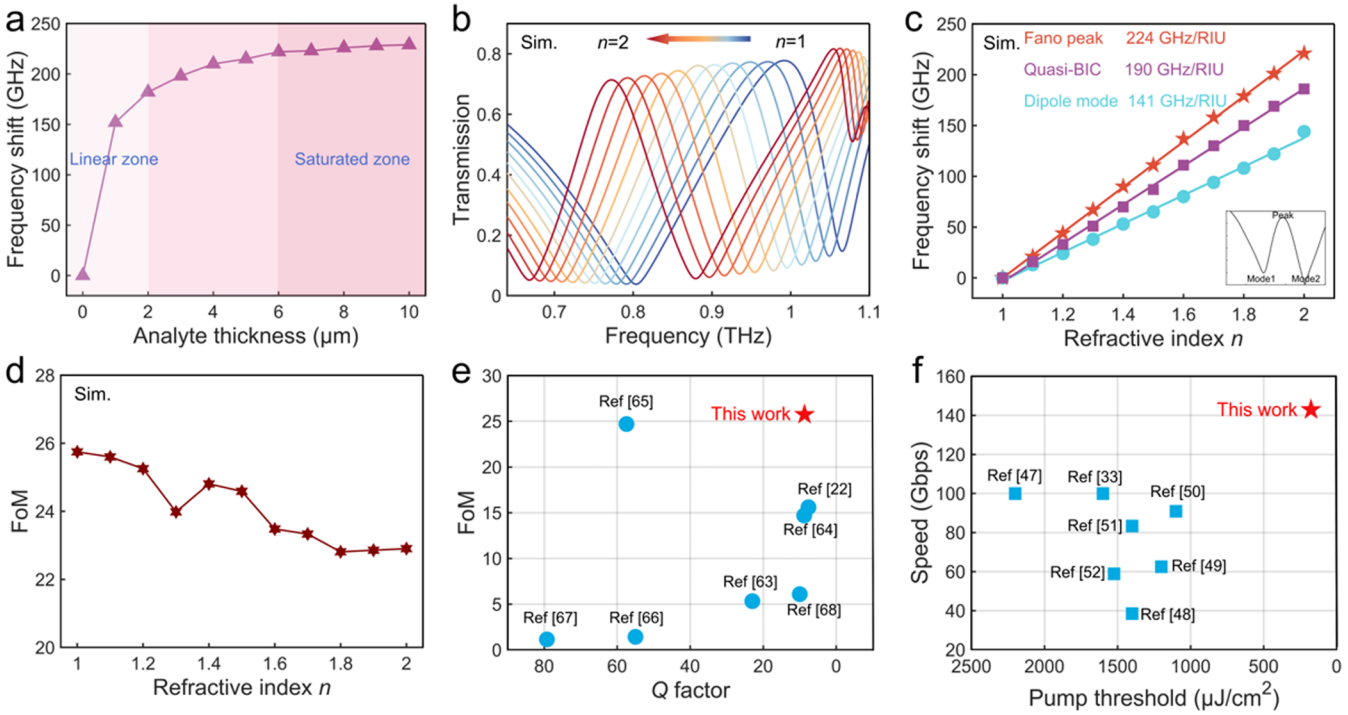

Figure 6. High-sensitive THz refractive index sensing and performance comparison. (a) The frequency shift of the Fano peak versus the analyte's thickness when the refractive index changes from 1 to 2. Upon the analyte with a thickness of 6 μm, (b) the transmission spectrum experiences a rapid red shift with the increase in the analyte's refractive index from 1 to 2. (c) The frequency shifts of Fano peak, dipole mode, and quasi-BIC are 224, 141, and 190 GHz/RIU, respectively, which are linearly increased with the refractive index. (d) FoM vs refractive index. Performance comparison with analogous studies in terms of (e) Q factor and FoM and (f) pump threshold, and switching speed.

density and the intensity of resonances. The proposed metasurface, while not characterized by a high-Q factor, demonstrates a significantly enhanced field, which boosts the light−matter interactions, also beneficial to sensing performance. Subsequently, we present the ultrasensitive sensing capabilities of the metasurfaces via numerical simulations.

As evidenced by prior research,[60−62] variations in the analyte material's refractive index or thickness effectively perturb the metasurface's local electromagnetic surroundings, consequently giving rise to measurable shifts in its resonance frequency. These shifts indicate the analyte properties and are vital to the sensing approach. As shown in Figure 1a, the analyte, with its refractive index ranging from 1 to 2, is uniformly coated onto the metasurface. Upon increasing the analyte thickness from 0 to 2 μm, there is a marked increase in the frequency shift $(f_{n=1} - f_{n=2})$ of the Fano resonance peak, an interval that we identify as the "linear zone." Subsequently, when the analyte thickness extends from 2 to 6 μm, the frequency shift experiences a gradual deceleration in its rate of increase. Upon reaching a thickness greater than 6 μm, the frequency shift virtually plateaus, indicating the transition into the so-called "saturated zone," as shown in Figure 6a.

The amplified electric field concentrated around the gap region significantly boosts the interaction between the light and analyte, accounting for the swift rise in the frequency shift within the "linear zone." Nonetheless, once the analyte thickness exceeds the region where the field enhancement effect is most pronounced in the z-direction, the excess analyte no longer experiences substantial interaction with the localized electric field. Consequently, the contribution of additional analyte layers to the frequency shift becomes negligible or nil, thus marking the entrance into the "saturated zone." When the analyte is present with a saturated thickness of 6 μm and its refractive index is varied from 1 to 2 at a step of 0.1, the transmission spectrum experiences a red shift with the increase in refractive index, as shown in Figure 6b.

To evaluate the sensor responsiveness quantitatively, we define the sensing sensitivity $S_{sense} = \Delta f/\Delta n$ as the frequency shift per unit change in the refractive index. The corresponding S_{sense} of the Fano peak, dipole mode, and quasi-BIC are 224 GHz/RIU, 141 GHz/RIU, and 190 GHz/RIU, respectively, obtained by the least-squares fit, as shown in Figure 6c. Besides, the effective mode volumes of the coupled dipole mode and quasi-BIC are 7.35 and 94.5 μm^3, respectively (Supporting Information Note 3). Additionally, to highlight this metasurface sensor's low-Q yet sensitive properties, we define figures of merit (FoM) = $S_{sense}/Q(n)$, where $Q(n)$ is the Q factor of the resonance concerning the refractive index n. The calculated FoM of the Fano peak decreases from 25.7 to 23, with the refractive index increasing from 1 to 2, as shown in Figure 6d. We compare other THz sensors with this work regarding the Q factor and FoM,[22,63−68] as shown in Figure 6e. Furthermore, a more comprehensive comparison across different studies is given in Table S1 (Supporting Information Note 4), encompassing aspects such as resonant types, working frequencies, Q factors, sensing sensitivity, figures of merit (FoM), and effective mode volumes.

Our proposed metasurface sensor has excellent potential for advantages in low-Q ultrasensitive sensing, providing a system-friendly paradigm for THz sensors. The high sensitivity of this metasurface to changes in the refractive index, combined with its low-Q property, allows for the precise detection of even

https://doi.org/10.1021/acsnano.4c04565
ACS Nano 2024, 18, 21211−21220

minute variations in chemical compositions or in the presence of biomolecules.

CONCLUSIONS

Our proposed quasi-BIC plasmonic metasurface, featuring a low-Q factor, showcases high sensitivity in ultrafast switching and sensing applications. The theoretical foundation of our design lies in the discovery that a pivotal requirement for achieving a low-Q resonator with heightened sensitivity to nonradiative losses is to facilitate strong coupling between high-Q and low-Q modes. Based on this physical mechanism, we have engineered a quasi-BIC metasurface wherein the nanogaps play a pivotal role in facilitating enhanced coupling between the quasi-BIC and dipole modes. This coupling effect results in not only a reduction of the Q factor of quasi-BIC but also near-field electric enhancement. Then, we successfully engineered a Ge-hybrid plasmonic metasurface. Experimental results reveal that the pump threshold for switching is as low as 192 $\mu J/cm^2$, an order of magnitude reduction compared to preceding Ge-based THz metasurfaces. Moreover, the ultrafast switching cycle of the metasurface has been measured at an exceptionally brief 7 ps. Furthermore, we have thoroughly explored the potential applications of this metasurface, confirming its efficacy as a low-Q and high-sensitivity refractive index sensor, which can realize the maximal sensitivity of 224 GHz/RIU. Our study has thus not only demonstrated a significant advancement in the design and functionality of THz metasurfaces with high sensitivity but also laid the groundwork for their diverse applications.

METHODS

Sample Fabrication. During the fabrication process, the z-cut quartz substrate was first cleaned by using an ultrasonic cleaning mixture of acetone and isopropanol. Subsequently, a 100 nm-thick silicon dioxide layer was deposited on the substrate surface using plasma-enhanced chemical vapor deposition. Following that, Ge (300 nm, Shenzhen six Carbon Technology Co., Ltd.), chromium (10 nm), and gold (200 nm) were sequentially deposited on the silicon dioxide surface using magnetron sputtering. The surface metal was then patterned using a stepper lithography machine and metal etching using an ion beam etching machine. Finally, the patterned photoresist was removed.

THz Time-Domain Spectroscopy and Optical Pump Measurements. The laser source of the home-built optical pump THz measurement system is a femtosecond laser with a central wavelength of 800 nm, a spectral width of 40 nm, a repetition rate of 1 kHz, and a pulse width of 100 fs. The THz signal's generation and detection are realized using two 1 mm-thick ZnTe crystals ⟨110⟩. After passing through the beam splitter, the 800 nm light beam is divided into three parts: the first part is used to generate the THz pulse by the second-order nonlinear effect of ZnTe; the second part is used to detect the modulated THz signal passing through the metasurface and focused on another ZnTe crystal; the third part is used to be an excitation for photocarrier generation in Ge. THz signal detection is based on electric field time domain scanning technology. By changing the time of the femtosecond laser to reach the detector, the THz signal is discretely sampled and then recovered. In optical pump measurement, the pump−probe time delay is controlled by moving the translational stage to measure the transient THz spectrum. Finally, the complex THz transmission spectrum was obtained by standard Fourier transform and substrate normalization.

Numerical Simulations. The data presented in Figure 3 were obtained through simulations conducted in COMSOL Multiphysics software, utilizing the finite element method (FEM) with periodic boundary conditions applied along the x- and y-directions, the plasmonic resonator was modeled as a perfect electric conductor layer, and no substrate was included to maintain the conditions of up−down mirror symmetry, which is very important to calculate the far-field polarization states near the BIC in momentum space. To mitigate the impact of backscattering on the resonance, a perfectly matching layer (PML) and appropriate boundary conditions were implemented on the interfaces of the additional spaces above and below the plasmonic structures. The eigenfrequency module in COMSOL was utilized to determine the eigenstates. The polarization states near the BIC are calculated by setting up the surface electric field integral of the far-field plane of the meta-atom. The transmission and reflection spectra were extracted from the input and output ports. Other simulation results were also extracted from CST Microwave Studio software, and unit cell boundaries along the x- and y-directions and open boundaries along the z-direction were employed. The electrical conductivity of lossy gold materials was set to be 4.52×10^7 S/m in the THz regime, and the quartz substrate and Ge material were set as a normal dielectric with a permittivity of 3.92 and 16.

ASSOCIATED CONTENT

Supporting Information

The Supporting Information is available free of charge at https://pubs.acs.org/doi/10.1021/acsnano.4c04565.

Transmission coefficients derived from coupled-mode theory; OPTP measurements of ultrafast photocarrier dynamics of amorphous Ge film; effective mode volume of the metasurface resonant cavity; and a detailed comparison with other THz sensors (PDF)

AUTHOR INFORMATION

Corresponding Authors

Yuze Hu − *Institute for Quantum Science and Technology, College of Science, National University of Defense Technology, Changsha 410073, China*; Email: hyz_yj@sina.com

Zhongjie Xu − *College of Advanced Interdisciplinary Studies, National University of Defense Technology, Changsha 410073, China*; Email: zhongjie_xu@qq.com

Tian Jiang − *Institute for Quantum Science and Technology, College of Science, National University of Defense Technology, Changsha 410073, China*; orcid.org/0000-0003-3343-5548; Email: tjiang@nudt.edu.cn

Authors

Ziheng Ren − *College of Advanced Interdisciplinary Studies, National University of Defense Technology, Changsha 410073, China*

Weibao He − *College of Advanced Interdisciplinary Studies, National University of Defense Technology, Changsha 410073, China*

Shun Wan − *College of Advanced Interdisciplinary Studies, National University of Defense Technology, Changsha 410073, China*

Siyang Hu − *College of Advanced Interdisciplinary Studies, National University of Defense Technology, Changsha 410073, China*

Zhongyi Yu − *College of Advanced Interdisciplinary Studies, National University of Defense Technology, Changsha 410073, China*

Xiang'ai Cheng − *College of Advanced Interdisciplinary Studies, National University of Defense Technology, Changsha 410073, China*

Complete contact information is available at: https://pubs.acs.org/10.1021/acsnano.4c04565

Author Contributions

Z.R. and Y.H. conceived the idea. Z.R. and S.W. designed the experiment and performed active measurements and all the simulations. S.H., W.H., and Z.Y. fabricated the samples. Z.R., Y.H., and S.H. discussed and analyzed the measured data. Z.X., Y.H., and T.J. supervised the theory and the measurements. Z.R. prepared the manuscript with inputs from T.J. and Y.H.

Notes

The authors declare no competing financial interest.

ACKNOWLEDGMENTS

The work was supported by the National Natural Science Foundation of China (62075240 and 62305384), the National Key Research and Development Program of China (2020YFB2205800), and the Youth Innovation Talent Incubation Foundation of the National University of Defense Technology (2023-lxy-fhij-007).

REFERENCES

(1) Yesilkoy, F.; Arvelo, E. R.; Jahani, Y.; Liu, M.; Tittl, A.; Cevher, V.; Kivshar, Y.; Altug, H. Ultrasensitive Hyperspectral Imaging and Biodetection Enabled by Dielectric Metasurfaces. *Nat. Photonics* **2019**, *13*, 390−396.

(2) Zhang, X.; Liu, Y.; Han, J.; Kivshar, Y.; Song, Q. Chiral Emission from Resonant Metasurfaces. *Science* **2022**, *377*, 1215−1218.

(3) Shi, T.; Deng, Z.-L.; Geng, G.; Zeng, X.; Zeng, Y.; Hu, G.; Overvig, A.; Li, J.; Qiu, C.-W.; Alù, A.; Kivshar, Y. S.; Li, X. Planar Chiral Metasurfaces with Maximal and Tunable Chiroptical Response Driven by Bound States in the Continuum. *Nat. Commun.* **2022**, *13*, No. 4111.

(4) Huang, L.; Jin, R.; Zhou, C.; Li, G.; Xu, L.; Overvig, A.; Deng, F.; Chen, X.; Lu, W.; Alù, A.; Miroshnichenko, A. E. Ultrahigh-Q Guided Mode Resonances in an All-Dielectric Metasurface. *Nat. Commun.* **2023**, *14*, No. 3433.

(5) Hwang, M.-S.; Kim, H.-R.; Kim, J.; Yang, B.-J.; Kivshar, Y.; Park, H.-G. Vortex Nanolaser Based on a Photonic Disclination Cavity. *Nat. Photonics* **2024**, *18*, 286−293.

(6) Liu, Z.; Guo, T.; Tan, Q.; Hu, Z.; Sun, Y.; Fan, H.; Zhang, Z.; Jin, Y.; He, S. Phase Interrogation Sensor Based on All-Dielectric BIC Metasurface. *Nano Lett.* **2023**, *23*, 10441−10448.

(7) Che, Y.; Zhang, T.; Shi, T.; Deng, Z.-L.; Cao, Y.; Guan, B.-O.; Li, X. Ultrasensitive Photothermal Switching with Resonant Silicon Metasurfaces at Visible Bands. *Nano Lett.* **2024**, *24*, 576−583.

(8) Wang, C.; Fang, Z.; Yi, A.; Yang, B.; Wang, Z.; Zhou, L.; Shen, C.; Zhu, Y.; Zhou, Y.; Bao, R.; Li, Z.; Chen, Y.; Huang, K.; Zhang, J.; Cheng, Y.; Ou, X. High-Q Microresonators on 4H-Silicon-Carbide-on-Insulator Platform for Nonlinear Photonics. *Light Sci. Appl.* **2021**, *10*, No. 139.

(9) Luo, X.; Han, Y.; Du, X.; Chen, S.; Li, G. Robust Ultrahigh- Q Quasi-Bound States in the Continuum in Metasurfaces Enabled by Lattice Hybridization. *Adv. Opt. Mater.* **2023**, *11*, No. 2301130.

(10) Kumar, A.; Gupta, M.; Pitchappa, P.; Tan, T. C.; Chattopadhyay, U.; Ducournau, G.; Wang, N.; Chong, Y.; Singh, R. Active Ultrahigh-Q (0.2×10^6) THz Topological Cavities on a Chip. *Adv. Mater.* **2022**, *34*, No. 2202370.

(11) Bin-Alam, M. S.; Reshef, O.; Mamchur, Y.; Alam, M. Z.; Carlow, G.; Upham, J.; Sullivan, B. T.; Ménard, J.-M.; Huttunen, M. J.; Boyd, R. W.; Dolgaleva, K. Ultra-High-Q Resonances in Plasmonic Metasurfaces. *Nat. Commun.* **2021**, *12*, No. 974.

(12) Le-Van, Q.; Zoethout, E.; Geluk, E.; Ramezani, M.; Berghuis, M.; Gómez Rivas, J. Enhanced Quality Factors of Surface Lattice Resonances in Plasmonic Arrays of Nanoparticles. *Adv. Opt. Mater.* **2019**, *7*, No. 1801451.

(13) Kravets, V. G.; Kabashin, A. V.; Barnes, W. L.; Grigorenko, A. N. Plasmonic Surface Lattice Resonances: A Review of Properties and Applications. *Chem. Rev.* **2018**, *118*, 5912−5951.

(14) Wang, B.; Yu, P.; Wang, W.; Zhang, X.; Kuo, H.; Xu, H.; Wang, Z. M. High-Q Plasmonic Resonances: Fundamentals and Applications. *Adv. Opt. Mater.* **2021**, *9*, No. 2001520.

(15) Zhang, X. C.; Shkurinov, A.; Zhang, Y. Extreme Terahertz Science. *Nat. Photonics* **2017**, *11*, 16−18.

(16) Jia, R.; Kumar, S.; Tan, T. C.; Kumar, A.; Tan, Y. J.; Gupta, M.; Szriftgiser, P.; Alphones, A.; Ducournau, G.; Singh, R. Valley-Conserved Topological Integrated Antenna for 100-Gbps THz 6G Wireless. *Sci. Adv.* **2023**, *9*, No. eadi8500.

(17) Yang, Y.; Yamagami, Y.; Yu, X.; Pitchappa, P.; Webber, J.; Zhang, B.; Fujita, M.; Nagatsuma, T.; Singh, R. Terahertz Topological Photonics for On-Chip Communication. *Nat. Photonics* **2020**, *14*, 446−451.

(18) Li, X.; Li, J.; Li, Y.; Ozcan, A.; Jarrahi, M. High-Throughput Terahertz Imaging: Progress and Challenges. *Light Sci. Appl.* **2023**, *12*, No. 233.

(19) Wang, X.-k.; Ye, J.; Sun, W.; Han, P.; Hou, L.; Zhang, Y. Terahertz Near-Field Microscopy Based on an Air-Plasma Dynamic Aperture. *Light Sci. Appl.* **2022**, *11*, No. 129.

(20) Tzydynzhapov, G.; Gusikhin, P.; Muravev, V.; Dremin, A.; Nefyodov, Y.; Kukushkin, I. New Real-Time Sub-Terahertz Security Body Scanner. *J. Infrared, Millimeter, Terahertz Waves* **2020**, *41*, 632−641.

(21) Tan, T. C.; Srivastava, Y. K.; Ako, R. T.; Wang, W.; Bhaskaran, M.; Sriram, S.; Al-Naib, I.; Plum, E.; Singh, R. Active Control of Nanodielectric-Induced THz Quasi-BIC in Flexible Metasurfaces: A Platform for Modulation and Sensing. *Adv. Mater.* **2021**, *33*, No. 2100836.

(22) Jiao, Y.; Lou, J.; Ma, Z.; Cong, L.; Xu, X.; Zhang, B.; Li, D.; Yu, Y.; Sun, W.; Yan, Y.; Hu, S.; Liu, B.; Huang, Y.; Sun, L.; Wang, R.; Singh, R.; Fan, Y.; Chang, C.; Du, X. Photoactive Terahertz Metasurfaces for Ultrafast Switchable Sensing of Colorectal Cells. *Mater. Horiz.* **2022**, *9*, 2984−2992.

(23) Yao, J.; Ou, J.-Y.; Savinov, V.; Chen, M. K.; Kuo, H. Y.; Zheludev, N. I.; Tsai, D. P. Plasmonic Anapole Metamaterial for Refractive Index Sensing. *PhotoniX* **2022**, *3*, No. 23.

(24) Yan, X.; Yang, M.; Zhang, Z.; Liang, L.; Wei, D.; Wang, M.; Zhang, M.; Wang, T.; Liu, L.; Xie, J.; Yao, J. The Terahertz Electromagnetically Induced Transparency-like Metamaterials for Sensitive Biosensors in the Detection of Cancer Cells. *Biosens. Bioelectron.* **2019**, *126*, 485−492.

(25) Ma, L.; Shi, W.; Fan, F.; Zhang, Z.; Zhang, T.; Liu, J.; Wang, X.; Chang, S. Terahertz Polarization Sensing, Chirality Enhancement, and Specific Binding Based on Metasurface Sensors for Biochemical Detection: A Review [Invited]. *Chin. Opt. Lett.* **2023**, *21*, No. 110003.

(26) Tian, H. W.; Shen, H. Y.; Zhang, X. G.; Li, X.; Jiang, W. X.; Cui, T. J. Terahertz Metasurfaces: Toward Multifunctional and Programmable Wave Manipulation. *Front. Phys.* **2020**, *8*, No. 584077.

(27) Zhang, J. C.; Wu, G.-B.; Chen, M. K.; Liu, X.; Chan, K. F.; Tsai, D. P.; Chan, C. H. A 6G Meta-Device for 3D Varifocal. *Sci. Adv.* **2023**, *9*, No. eadf8478.

(28) Hu, Y.; Tong, M.; Hu, S.; He, W.; Cheng, X.; Jiang, T. Spatiotemporal Lineshape Tailoring in BIC-Mediated Reconfigurable Metamaterials. *Adv. Funct. Mater.* **2022**, *32*, No. 2203680.

(29) Hu, Y.; Tong, M.; Hu, S.; He, W.; Cheng, X.; Jiang, T. Reassessing Fano Resonance for Broadband, High-Efficiency, and Ultrafast Terahertz Wave Switching. *Adv. Sci.* **2023**, *10*, No. 2204494.

(30) Gu, T.; Kim, H. J.; Rivero-Baleine, C.; Hu, J. Reconfigurable Metasurfaces towards Commercial Success. *Nat. Photonics* **2023**, *17*, 48−58.

(31) Manjappa, M.; Srivastava, Y. K.; Cong, L.; Al-Naib, I.; Singh, R. Active Photoswitching of Sharp Fano Resonances in THz Metadevices. *Adv. Mater.* **2017**, *29*, No. 1603355.

(32) Cong, L.; Srivastava, Y. K.; Zhang, H.; Zhang, X.; Han, J.; Singh, R. All-Optical Active THz Metasurfaces for Ultrafast Polarization Switching and Dynamic Beam Splitting. *Light Sci. Appl.* **2018**, *7*, No. 28.

(33) Lou, J.; Xu, X.; Huang, Y.; Yu, Y.; Wang, J.; Fang, G.; Liang, J.; Fan, C.; Chang, C. Optically Controlled Ultrafast Terahertz

https://doi.org/10.1021/acsnano.4c04565
ACS Nano 2024, 18, 21211−21220

Metadevices with Ultralow Pump Threshold. *Small* **2021**, *17*, No. 2104275.
(34) Li, W.; Chen, B.; Hu, X.; Guo, H.; Wang, S.; Wu, J.; Fan, K.; Zhang, C.; Wang, H.; Jin, B.; Chen, J.; Wu, P. Modulo-Addition Operation Enables Terahertz Programmable Metasurface for High-Resolution Two-Dimensional Beam Steering. *Sci. Adv.* **2023**, *9*, No. eadi7565.
(35) Chen, B.; Wang, X.; Li, W.; Li, C.; Wang, Z.; Guo, H.; Wu, J.; Fan, K.; Zhang, C.; He, Y.; Jin, B.; Chen, J.; Wu, P. Electrically Addressable Integrated Intelligent Terahertz Metasurface. *Sci. Adv.* **2022**, *8*, No. eadd1296.
(36) Chen, B.; Wu, J.; Li, W.; Zhang, C.; Fan, K.; Xue, Q.; Chi, Y.; Wen, Q.; Jin, B.; Chen, J.; Wu, P. Programmable Terahertz Metamaterials with Non-Volatile Memory. *Laser Photonics Rev.* **2022**, *16*, No. 2100472.
(37) Li, Q.; Tian, Z.; Zhang, X.; Singh, R.; Du, L.; Gu, J.; Han, J.; Zhang, W. Active Graphene−Silicon Hybrid Diode for Terahertz Waves. *Nat. Commun.* **2015**, *6*, No. 7082.
(38) Hu, Y.; Tong, M.; Xu, Z.; Cheng, X.; Jiang, T. Bifunctional Spatiotemporal Metasurfaces for Incident Angle-Tunable and Ultrafast Optically Switchable Electromagnetically Induced Transparency. *Small* **2021**, *17*, No. 2006489.
(39) Cong, L.; Singh, R. Spatiotemporal Dielectric Metasurfaces for Unidirectional Propagation and Reconfigurable Steering of Terahertz Beams. *Adv. Mater.* **2020**, *32*, No. 2001418.
(40) Liu, J.; Fan, F.; Tan, Z.; Zhao, H.; Cheng, J.; Chang, S. Active Terahertz-Beam Deflection in a Double-Sided All-Dielectric Metadevice Modulated by Both Polarization Rotation and Optical Pumping. *Phys. Rev. Appl.* **2023**, *19*, No. 054086.
(41) He, W.; Cheng, X.; Hu, S.; Ren, Z.; Yu, Z.; Wan, S.; Hu, Y.; Jiang, T. Color Coded Metadevices toward Programmed Terahertz Switching. *Light Sci. Appl.* **2024**, *13*, No. 142.
(42) Cai, H.; Chen, S.; Zou, C.; Huang, Q.; Liu, Y.; Hu, X.; Fu, Z.; Zhao, Y.; He, H.; Lu, Y. Multifunctional Hybrid Metasurfaces for Dynamic Tuning of Terahertz Waves. *Adv. Opt. Mater.* **2018**, *6*, No. 1800257.
(43) Zeng, H.; Cong, X.; Wang, S.; Gong, S.; Huang, L.; Wang, L.; Liang, H.; Lan, F.; Cao, H.; Wang, Z.; Wang, W.; Liang, S.; Feng, Z.; Yang, Z.; Zhang, Y.; Cui, T. J. Ultrafast Modulable 2DEG Huygens Metasurface. *Photonics Res.* **2024**, *12*, 1004−1015.
(44) Zhuang, X.; Zhang, W.; Wang, K.; Gu, Y.; An, Y.; Zhang, X.; Gu, J.; Luo, D.; Han, J.; Zhang, W. Active Terahertz Beam Steering Based on Mechanical Deformation of Liquid Crystal Elastomer Metasurface. *Light Sci. Appl.* **2023**, *12*, No. 14.
(45) Xu, J.; Yuan, T.; Mickan, S.; Zhang, X.-C. Limit of Spectral Resolution in Terahertz Time-Domain Spectroscopy. *Chin. Phys. Lett.* **2003**, *20*, 1266−1268.
(46) Eliet, S.; Cuisset, A.; Hindle, F.; Lampin, J.-F.; Peretti, R. Broadband Super-Resolution Terahertz Time-Domain Spectroscopy Applied to Gas Analysis. *IEEE Trans. Terahertz Sci. Technol.* **2022**, *12*, 75−80.
(47) He, W.; Tong, M.; Xu, Z.; Hu, Y.; Cheng, X.; Jiang, T. Ultrafast All-Optical Terahertz Modulation Based on an Inverse-Designed Metasurface. *Photonics Res.* **2021**, *9*, 1099−1108.
(48) Hu, Y.; Hao, H.; Zhang, J.; Tong, M.; Cheng, X.; Jiang, T. Anisotropic Temporal Metasurfaces for Tunable Ultrafast Photoactive Switching Dynamics. *Laser Photonics Rev.* **2021**, *15*, No. 2100244.
(49) Hu, Y.; Tong, M.; Xu, Z.; Cheng, X.; Jiang, T. Spatiotemporal Terahertz Metasurfaces for Ultrafast All-Optical Switching with Electric-Triggered Bistability. *Laser Photonics Rev.* **2021**, *15*, No. 2000456.
(50) Hu, Y.; You, J.; Tong, M.; Zheng, X.; Xu, Z.; Cheng, X.; Jiang, T. Pump-Color Selective Control of Ultrafast All-Optical Switching Dynamics in Metaphotonic Devices. *Adv. Sci.* **2020**, *7*, No. 2000799.
(51) Hu, Y.; Tong, M.; Hu, S.; He, W.; Cheng, X.; Jiang, T. Multidimensional Engineered Metasurface for Ultrafast Terahertz Switching at Frequency-Agile Channels. *Nanophotonics* **2022**, *11*, 1367−1378.
(52) Lim, W. X.; Manjappa, M.; Srivastava, Y. K.; Cong, L.; Kumar, A.; MacDonald, K. F.; Singh, R. Ultrafast All-Optical Switching of Germanium-Based Flexible Metaphotonic Devices. *Adv. Mater.* **2018**, *30*, No. 1705331.
(53) Huang, W.; Lin, J.; Qiu, M.; Liu, T.; He, Q.; Xiao, S.; Zhou, L. A Complete Phase Diagram for Dark-Bright Coupled Plasmonic Systems: Applicability of Fano's Formula. *Nanophotonics* **2020**, *9*, 3251−3262.
(54) Fan, S.; Suh, W.; Joannopoulos, J. D. Temporal Coupled-Mode Theory for the Fano Resonance in Optical Resonators. *J. Opt. Soc. Am. A* **2003**, *20*, 569−572.
(55) Ye, W.; Gao, Y.; Liu, J. Singular Points of Polarizations in the Momentum Space of Photonic Crystal Slabs. *Phys. Rev. Lett.* **2020**, *124*, No. 153904.
(56) Jiang, Q.; Hu, P.; Wang, J.; Han, D.; Zi, J. General Bound States in the Continuum in Momentum Space. *Phys. Rev. Lett.* **2023**, *131*, No. 013801.
(57) Cui, Z.; Wang, Y.; Sun, G.; Chen, W.; Zhang, K.; Wang, X. Observation of the Bound States in the Continuum Supported by Mode Coupling in a Terahertz Metasurface. *Opt. Lett.* **2023**, *48*, 4809−4812.
(58) Yin, X.; Wang, Q.; Yang, N.; Yan, X.; Wang, L. All-Dielectric Metasurface Refractive Index Sensor with High Figure of Merit Based on Quasi-Bound States in the Continuum. *J. Phys. D: Appl. Phys.* **2023**, *56*, No. 485103.
(59) Strait, J. H.; George, P. A.; Levendorf, M.; Blood-Forsythe, M.; Rana, F.; Park, J. Measurements of the Carrier Dynamics and Terahertz Response of Oriented Germanium Nanowires Using Optical-Pump Terahertz-Probe Spectroscopy. *Nano Lett.* **2009**, *9*, 2967−2972.
(60) Qin, J.; Jiang, S.; Wang, Z.; Cheng, X.; Li, B.; Shi, Y.; Tsai, D. P.; Liu, A. Q.; Huang, W.; Zhu, W. Metasurface Micro/Nano-Optical Sensors: Principles and Applications. *ACS Nano* **2022**, *16*, 11598−11618.
(61) Ahmadivand, A.; Gerislioglu, B.; Ahuja, R.; Mishra, Y. K. Terahertz Plasmonics: The Rise of Toroidal Metadevices towards Immunobiosensings. *Mater. Today* **2020**, *32*, 108−130.
(62) Ahmadivand, A.; Gerislioglu, B. Photonic and Plasmonic Metasensors. *Laser Photonics Rev.* **2022**, *16*, No. 2100328.
(63) Ding, J.; Huang, L.; Luo, Y.; Wang, T.; Hu, J.; Li, R.; Xiao, S. Multi-Band Polarization-Independent Quasi-Bound States in the Continuum Based on Tetramer-Based Metasurfaces and Their Potential Application in Terahertz Microfluidic Biosensing. *Adv. Opt. Mater.* **2023**, *11*, No. 2300685.
(64) Xu, J.; Liao, D.; Gupta, M.; Zhu, Y.; Zhuang, S.; Singh, R.; Chen, L. Terahertz Microfluidic Sensing with Dual-Torus Toroidal Metasurfaces. *Adv. Opt. Mater.* **2021**, *9*, No. 2100024.
(65) Chen, X.; Fan, W. Ultrasensitive Terahertz Metamaterial Sensor Based on Spoof Surface Plasmon. *Sci. Rep.* **2017**, *7*, No. 2092.
(66) Qu, Z.; Kang, J.; Li, W.; Yao, B.; Deng, H.; Wei, Y.; Jing, H.; Li, X.; Duan, J.; Zhang, B. Microstructure-Based High-Quality Factor Terahertz Metamaterial Bio-Detection Sensor. *Adv. Compos. Hybrid Mater.* **2023**, *6*, No. 100.
(67) Guo, W.; Zhai, L.; El-Bahy, Z. M.; Lu, Z.; Li, L.; Elnaggar, A. Y.; Ibrahim, M. M.; Cao, H.; Lin, J.; Wang, B. Terahertz Metamaterial Biosensor Based on Open Square Ring. *Adv. Compos. Hybrid Mater.* **2023**, *6*, No. 92.
(68) Gupta, M.; Singh, R. Terahertz Sensing with Optimized Q/V_{eff} Metasurface Cavities. *Adv. Opt. Mater.* **2020**, *8*, No. 1902025.

https://doi.org/10.1021/acsnano.4c04565
ACS Nano 2024, 18, 21211−21220